PHYSICAL REVIEW A VOLUME 46, NUMBER 8 15 OCTOBER 1992

Comparison of steady-state and strongly chaotic thermal convection at high Rayleigh number

U. Hansen*
Institut für Geophysik und Meteorologie, Universität zu Köln, D-5000 Köln 41, Germany

D. A. Yuen and A. V. Malevsky
Minnesota Supercomputer Institute, Army High Performance Computing Research Center and Department of Geology and Geophysics, Univerity of Minnesota, Minneapolis, Minnesota 55415

(Received 16 October 1991; revised manuscript received 13 April 1992)

Steady-state and time-dependent two-dimensional thermal convection in a Boussinesq, infinite-Prandtl-number fluid with stress-free boundaries has been investigated. Two independent numerical methods have been employed to calculate the evolution of convective flows in a rectangular box with aspect ratio $\lambda=1.8$ in a Rayleigh-number (Ra) range of $10^6<\mathrm{Ra}<10^9$. With increasing Ra, greater than 10^7, the flow reveals the presence of disconnected thermals, rather than connected plumes, driven by a persistent large-scale circulation. Such features have also been reported from laboratory convection experiments in the regime of hard turbulence. Extensive calculations were performed (up to 140 overturns) in order to reach the statistically stationary regime for strongly chaotic flows. A Gaussian distribution with a mean value Nu_t was derived from the time history of the Nusselt (Nu) numbers. The value of Nu_t can be directly obtained by solving the steady-state equations via an iteration procedure. Thus the stationary flow obtained from the steady-state method resembles the turbulent flow in a statistical sense. Since the iteration procedure is about 10^4 times faster than calculating the full time-dependent evolution, it allows for the systematic investigation of the heat-transfer Nu-Ra relationship and other types of scaling laws. The steady-state and time-dependent experiments indicate that a power-law exponent of $\beta=0.315$ holds for the Nu-Ra relation for stress-free boundaries in the entire range of Ra. No indication of a jump in the exponent was found in the transition to hard turbulence.

PACS number(s): 47.25.Qv, 47.20.Tg, 47.25.Ae

I. INTRODUCTION

The phenomenon of thermal convection at high Rayleigh numbers has received increasing attention during the past several years, especially since a transition from a state of "soft turbulence" to "hard turbulence" has been reported [1,2]. Laboratory [3,4] and numerical studies [5,6] have demonstrated that large-scale flows (henceforth, LSC) persist in turbulent convection. The interaction of such a "wind" generated by the large-scale circulation and the instabilities originating in the thermal boundary layers is believed to play a key role in hard turbulence [2]. While classical theory [7–9] predicts the Nusselt number Nu to increase as $\mathrm{Ra}^{1/3}$ or the boundary-layer thickness δ to decrease as $\delta\sim 1/\mathrm{Ra}^{1/3}$, Castaing *et al.* [2] obtained an exponent of $\beta=0.289$ in the regime of hard turbulence, which is lower than the classical value. The classical approach is based on the assumption that the boundary-layer thickness is determined by marginal stability [7]. The idea was proposed that boundary layers can be stabilized [2] by the shearing wind, thus increasing the thickness of δ and decreasing Nu. The shear-induced stabilization for δ is the key to understanding of the transition from soft to hard turbulence [2]. Besides a decrease in the Nusselt number, a change in the probability distribution functions (PDF's) of temperature fluctuations from Gaussian to exponential shape has been proposed to be characteristic of the transition to hard turbulence [2,10,11]. However, both the transition of the power-law index β and the change from Gaussian to exponential shape in the PDF across the transition to hard turbulence have been called into question [12]. Numerical experiments [13] indicated a kink in the Nu-Ra relation but did not show any evidence for a change in the PDF's. Laboratory experiments [12] have reported the absence of a transition in the scaling exponent. They also found a dependence of the shape of the PDF's on the aspect ratio of the flow, thus questioning the universality of the PDF's. Earlier, it was demonstrated [14] that an induced shear stabilization was unlikely to cause a decrease of the scaling exponent. From the absence of a clear change in the PDF's at the transition from soft to hard turbulence, they concluded that an analysis of the global structures of the temperature and velocity fields, rather than only a local analysis of temperature fluctuations, was needed for a deeper understanding of the nature of this transition.

Up to now, any global analysis of the flow field has been restricted to a qualitative level. Sano, Wu, and Libchaber [4] and Solomon and Gollub [12,14] have observed thermals which are connected from the bottom to the top in the soft turbulent regime, but which break down into pieces before they can traverse the entire layer at higher values of Ra. The same phenomenon was found in two-dimensional (2D) experiments [6] on convection at high Ra in fluids with infinite Prandtl number Pr. By using computer animation and video techniques, they were able to show a transition form predominantly connected plumes [6] to disconnected, dropletlike structures (Ref. 15)]. There is much evidence to support this view that it is this change in the behavior of the plumes which constitutes the underlying mechanism for the transition from soft to hard turbulence [4,6,12,14,16].

With numerical experiments one can easily conduct global analysis of the flow field with graphics workstations (see Ref. [17]). However, many technical difficulties are encountered even with the present generation of supercomputers. A complete global analysis of a rapidly fluctuating velocity and temperature field requires the storage and the processing of enormous amounts of data with $O(10$ to 10^2 Gbytes), thus pushing the computational resources to their limits. This is the prime reason why in most of the numerical studies on this transition, the detailed evolution of the physical fields was not displayed, with the exception of the two-dimensional works [6,15,18]. Numerical computations are different in nature from laboratory experiments and they are very costly in computational time to produce time series with $O(10^2)$ overturns which are long enough to be statistically stationary [19]. Such times series are needed in order to obtain meaningful scaling relations such as Nu versus Ra. Balachandar and Sirovich [10] have pointed out the importance of sufficiently long time series for the shape of the PDF's. They presented results for three-dimensional (3D) simulations which were run for about 40 overturns. But this study was also limited to a single Ra, thus not allowing the determination of the Nu-Ra dependence. The basic physics of hard turbulent convection, such as the appearance of disconnected plumes, can be found also in two-dimensional simulations [6]. They have the advantage of being easier to obtain computationally and the ability to reach much higher Ra than 3D simulations.

In this study we will present several 2D simulations, spanning a range of Rayleigh numbers between 10^6 and 10^9. Several of them have been run for more than 120 overturn times; such an undertaking would not be easily done for 3D simulations with the present generation of vector supercomputers. We have focused our attention on thermal convection in a Boussinesq fluid at infinite Prandtl number. This type of flow is of important relevance for thermal convection in planetary interiors. In particular, an iteration scheme will be described, which allows for obtaining steady-state solutions to the advective-diffusive equations at high Ra. Next we will investigate the properties of this type of convection and study the relationships between stationary and time-dependent convective flows. Two-dimensional turbulent flows for the Euler equations have recently been studied by an equilibrium statistical-mechanical approach [20].

II. MODEL DESCRIPTION AND MATHEMATICAL METHODS

As a model configuration, we used a two-dimensional rectangular box, filled with a Boussinesq and infinite-Prandtl-number fluid. The system is subject to stress-free boundary conditions along all four sides. The temperature is fixed at the bottom and the top, and the sidewalls are thermally insulated. After scaling to nondimensional values, one obtains with the stream function ψ, which is used to enforce the continuity equation. The momentum equation is

$$\nabla^4\psi = Ra\frac{\partial T}{\partial x} \tag{1}$$

and the energy equation for a bottom-heated configuration is

$$\frac{\partial T}{\partial t} = \nabla^2 T + \frac{\partial \psi}{\partial x}\frac{\partial T}{\partial z} - \frac{\partial \psi}{\partial z}\frac{\partial T}{\partial x} , \tag{2}$$

where

$$Ra = \alpha g \Delta T d^3/\kappa\nu$$

denotes the Rayleigh number for a base-heated system. Here, α is the coefficient of thermal expansion, g is the acceleration of gravity, ΔT is the temperature difference across the layer, d is the depth of the layer, κ is thermal diffusivity, and ν is the kinematic viscosity. T denotes the nondimensional temperature, t the time, nondimensionalized by the thermal-diffusion time across the layer x, z the horizontal and vertical coordinates with the z axis pointing upward, and u and w the horizontal and vertical velocities. The momentum equation does not contain time dependence because of the creeping-flow nature of the mantle.

The system of equations (Eqs. (1) and (2)] is discretized in space by a finite-element technique [21]. A predictor-corrector method, second-order correct, is employed to advance T in time. We note that the energy equation contains the sole time dependence and nonlinearity in the thermal advection time. The finite-element technique offers two essential advantages. First, local grid refinement can easily be handled in order to resolve temperature gradients with the boundary layers properly. Second, local upwind schemes, used to damp out numerically induced oscillations, can be chosen to be much more effective on the local velocity field than for finite-difference methods [22]. The method has been checked carefully in an extensive benchmark study [23]. In this study we have also employed an independent method described below.

The second method, based on the method of characteristics [18], has also been employed in this study. In this case both stream-function and temperature fields were approximated by bicubic splines. The high order of this numerical scheme ensures the stability of the characteristics-based scheme, where the algorithm incorporates a spatial interpolation at each time step. A second-order predictor-corrector scheme was used for the time stepping. The method of characteristics enables us to employ time steps larger than those defined by the Courant criterion. The accuracy of this characteristics-based scheme was verified [18] on the standard benchmark test for infinite-Prandtl-number thermal convection.

We can use a different procedure for calculating solutions of the steady-state convection equations. By setting the term $\partial T/\partial t$ to zero in Eq. (2), any possibility for time dependence has been removed from the system. The time-stepping scheme is then replaced by an iteration procedure. Starting with a given temperature field, the velocities are calculated from Eq. (1), and with this new velocity, the temperature is updated from the steady-state temperature equation which reads

$$\nabla^2 T + \frac{\partial\psi}{\partial x}\frac{\partial T}{\partial z} - \frac{\partial\psi}{\partial z}\frac{\partial T}{\partial x} = 0 \ . \tag{3}$$

The iteration process is terminated for, and the following global convergence criterion is imposed:

$$\sum_{i=1}^{N} [(T^{n+1} - T^{n})^2/(T^{n})^2]^{1/2} < \epsilon \tag{4a}$$

and

$$\sum_{i=1}^{N} [(\mathbf{u}^{n+1} - \mathbf{u}^{n})^2/(\mathbf{u}^{n})^2]^{1/2} < \epsilon \ , \tag{4b}$$

where ϵ is $O(10^{-6})$, N is the number of nodal points, and $\mathbf{u}$ denotes the vector of unknowns at each element point for the velocity field and is given by ψ and its spatial first derivatives with respect to x and z. Usually, 10 to 15 iterations are sufficient for achieving criteria imposed by Eq. (4). An underrelaxation procedure involving the linear combination of the $n+1$th and the nth iterations is needed at high Ra to facilitate convergence of the iteration scheme. In this study an underrelaxation parameter of 0.3 was used and about 10 to 15 iterations were found to be sufficient for achieving convergence as defined by Eq. (4).

Similar finite-element methods [22,24] have been used in mantle convection. Finite-difference [25] and Galerkin [26] methods have also been employed earlier for steady-state, infinite-Prandtl-number convection. With finite-element methods, a stationary solution can be obtained much faster compared to time-stepping schemes. Therefore, finite-element schemes are well suited for studying transport properties of steady-state convection. Details of the finite-element method can be found in Hansen and Ebel [22].

In the benchmark study [23], it has been demonstrated that the combined use of a nonuniform grid and underrelaxation procedure allows for fast and accurate computations of stationary solutions. In order to achieve the same accuracy with uniform grids, many more grid points are required [23]. Using a time-stepping procedure instead of the iteration procedure results in an increase of computational time by a factor of at least 10 000 or more.

Since there does not exist only one, unique solution to the stationary problem but rather a manifold of solutions at a given Rayleigh number, the iteration process does not necessarily converge to one steady-state solution. In general, the degeneracy of the solutions is greatly dictated by the aspect ratio of the computational domain. For small boxes only one stable steady state can be found—for example, in a square box—while a whole class of different steady-state patterns can be observed in larger domains [22].

In this study we will only be concerned with domains of aspect ratio 1.8. This seems to be a good compromise in that it offers sufficient degrees of freedom for the flow to exhibit its whole complex behavior but also in that we do not have to contend with the slowly varying changes of the large-scale circulation, as has been observed in larger boxes [6].

The convergence of the iteration procedure towards a steady state does not automatically guarantee that the stationary flow is stable against time-dependent perturbations. It is well known that, depending on the particular type of stationary flow, a small perturbation can cause a breakdown of the stationary convection, giving rise to time-dependent flows [21,26].

We will show in Sec. III that a steady-state flow represents a truly turbulent convection in an averaged sense. In other words, the statistical steady state for a turbulent flow can be directly obtained by the iteration procedure outlined above. This idea of statistical hydrodynamics is not new and goes back more than 40 years ago to Onsager [27].

III. NUMERICAL RESULTS

In this section we will examine the transport properties of two-dimensional stationary and turbulent convection. We will, in particular, investigate the statistical question as to how the solutions to the stationary convection problem are related to the corresponding time-dependent evolutions.

Figure 1 displays the contours of the nondimensional temperature T (a) and streamlines ψ (b) for stationary convection at a Rayleigh number of $\mathrm{Ra}=10^6$. The solution in a box with aspect ratio $\lambda=1.8$ has been obtained

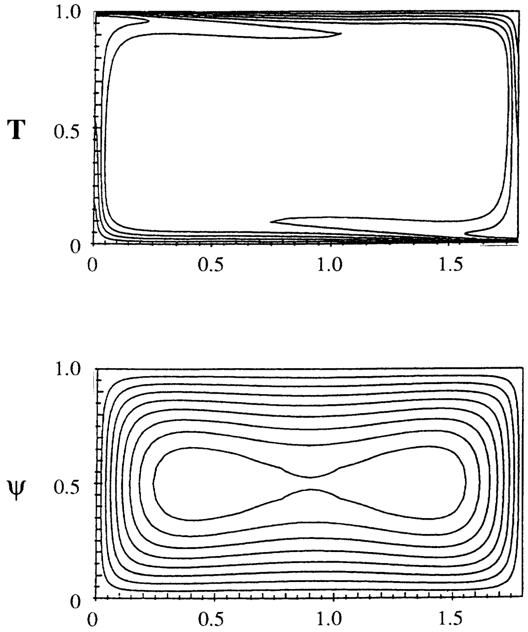

FIG. 1. Steady-state temperature T and stream function ψ fields for $\mathrm{Ra}=10^6$. A grid of 180×60 unevenly spaced points were used with the smallest elements being $\Delta x=\Delta z=0.001$. Finite-element code [21] is used here.

by iterating the stationary equations until convergence of ϵ is obtained [see Eq. (4)]. The stationary flow is characterized by an almost isothermal interior surrounded by thermal boundary layers with steep temperature gradients. Such types of steady-state flows have been used extensively in the geophysical literature in order to determine scaling laws for mantle heat transfer, mainly the dependence of Nu on Ra [24,27,28,29]. The Nusselt number is defined here to be the ratio of actual heat transport to the amount of heat transport which is due solely to conduction, i.e.,

$$\mathrm{Nu}=\frac{\overline{wT}-K\overline{\frac{\partial T}{\partial z}}}{K\frac{\Delta T}{d}} , \tag{5}$$

where w denotes the vertical velocity and overbars indicate horizontal averages, or for the dimensionless values used here,

$$\mathrm{Nu}=\frac{1}{\lambda}\int_0^{\lambda}\left[wT-\frac{\partial T}{\partial z}\right]dx . \tag{6}$$

For a wide range of Ra, $10^6<\mathrm{Ra}<10^8$, most studies have found a power-law dependence [24,30,29] of the form

$$\mathrm{Na}\sim\mathrm{Ra}^{\beta} , \tag{7}$$

with β less than 0.32. Classical boundary-layer stability theory [7,31] predicts a diffusive boundary layer whose thickness δ is determined by marginal stability. Following classical theory, marginal stability can be expressed by a critical Rayleigh number associated with the boundary layer itself:

$$\mathrm{Ra}_{\delta}=\frac{\alpha g\Delta T_{\delta}\delta^3}{\kappa\nu} , \tag{8}$$

and with the assumption that the core of the convection cell is isothermal and the temperature drop occurs only across the boundary layers, one obtains the boundary-layer Rayleigh number

$$\mathrm{Ra}_{\delta}=\frac{\mathrm{Ra}\delta^3}{2d^3} \quad \text{with } \Delta T_{\delta}=\frac{\Delta T}{2} . \tag{9}$$

A boundary layer at marginal stability implies that Ra_{δ} remains constant at a certain critical value and therefore the boundary-layer thickness must vary as

$$\delta\sim\mathrm{Ra}^{-1/3} . \tag{10}$$

In the classical view, Nu can be expressed as

$$\mathrm{Nu}=\frac{d}{2\delta} , \tag{11}$$

leading to

$$\mathrm{Nu}\sim\mathrm{Ra}^{1/3} . \tag{12}$$

An exponent less than $\frac{1}{3}$ means that above a certain Ra, the thermal boundary layers will become too thick to remain stable. It has been argued that convection in infinite-Prandtl-number convection would become time dependent only at extremely high values of Ra [24,32], $\mathrm{Ra}>10^8$, because the scaling exponent was found to be slightly less than $\frac{1}{3}$.

In subsequent investigations [21,33], however, it was recognized that steady-state convection and chaotic time-fluctuating flows can coexist at the same value of Ra, depending just on initial conditions and the aspect ratio of the box. While stationary convection shows a significant stability against time-dependent disturbances in square boxes, time-dependent convection prevails in domains with larger aspect ratio [6]. The stability of stationary convection [29] up to very high Ra, $\mathrm{Ra}\sim10^{10}$, was only due to the restriction to a small aspect-ratio box and not at all due to the infinite Prandtl number. Figure 2 illustrates this point well. Under the same conditions as are given in Fig. 1, we have calculated the evolution of the flow from the conductive state with the time-stepping scheme, rather than using the iteration scheme. Two snapshots, taken at different time instants, demonstrate the typical behavior of the thermal field. The thermal boundaries are modulated by instabilities, traveling as waves [33,34] with the large-scale circulation. It has been shown in numerous studies that in fact time-dependent [21,33] convection is the typical type of convection at Ra higher than 10^5. Although time-dependent convection prevails, it is important to note that nontrivial solutions of the steady-state equations, as shown in Fig. 1, can also be obtained.

An increase of Ra to 10^8 does not change this picture. The iteration process converges towards a steady-state

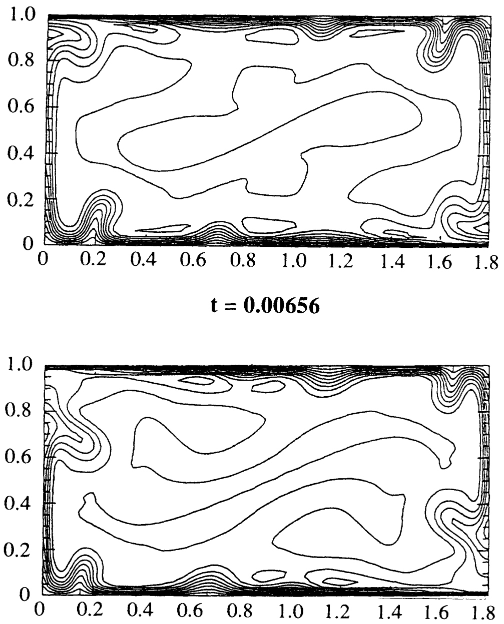

t = 0.00656

t = 0.00714

FIG. 2. Time-dependent snapshots of T for $\mathrm{Ra}=10^6$. The bicubic spline code was employed with 48×160 grid points, unevenly spaced in z and evenly spaced along x. Time is nondimensionalized with respect to the thermal-diffusion time across the layer.

solution, as displayed in Fig. 3. Compared to the solution for $Ra=10^6$, the thermal boundary layers are much thinner, whereas the streamlines show only minor changes with a tendency of the flow in the interior to form eddies [35]. The value of $Ra=10^8$ is beyond the threshold for the transition to hard turbulence [2]. One of the dominant characteristics of the hard turbulent regime is the occurrence of broken plumes, rather than thermal structures which are connected from the bottom to the top [4,6,12,14,15]. From the two snapshots taken from a time-dependent calculation for the same parameters, the appearance of disconnected plumes can be clearly observed (Fig. 4). Thermals erupt from the boundary layers but break down into droplets before they can reach the opposite boundary [Fig. 4(b)]. Besides the small-scale instabilities, there is also a LSC on the scale of the width of the box. Thermals from the bottom and top boundary layers are given in opposite direction by LSC, similar to the behavior described in Ref. [3]. Another characteristic feature of this type of convection is the collision of boundary-layer instabilities prior to their collective eruption. This merging phenomenon, which has also been observed in laboratory experiments [14] and three-dimensional numerical experiments [36], is discussed in Vincent *et al.* [15]. Further details on this plume collision phenomenon, which is similar to vortex merging [37] in atmospheric dynamics, can be found in Refs. [6] and [16].

In order to determine how the stationary flows are related to the time-dependent flows, it is reasonable to compare the Nusselt numbers. Both cases, for $Ra=10^6$ and $Ra=10^8$, show a striking agreement of the Nusselt number as calculated from the steady-state Nu_s and the time-averaged Nusselt number Nu_t. From the steady states we find a value of $Nu_s=17.3$ and $Nu_s=72.0$ for $Ra=10^6$ and 10^8, respectively, while for the time-dependent calculations, we have determined $Nu_t=17.2$ and 71. This coincidence of the two Nu numbers suggests that the stationary state, as obtained by iterating the time-independent equations, indeed resembles the statistically stationary value Nu_t from a time-dependent evolution.

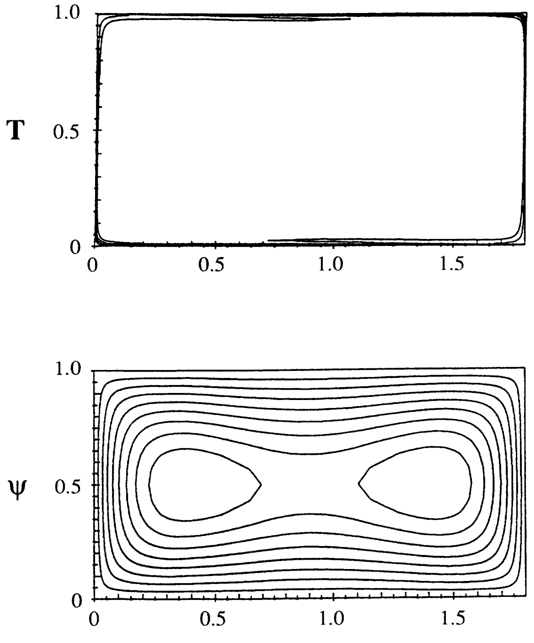

FIG. 3. Same as in Fig. 1, but $Ra=10^8$.

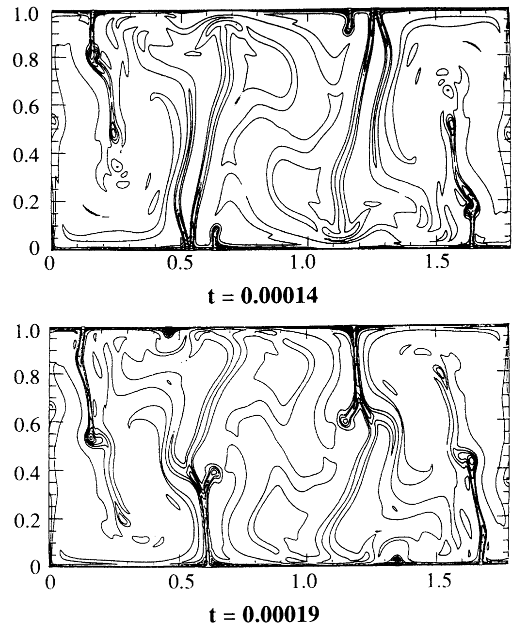

FIG. 4. Same as in Fig. 2, but $Ra=10^8$ and a mesh of 140×400 bicubic spline grid points.

Before comparing the results for a wider range of Rayleigh numbers, we will discuss the possible sources for errors. The numerical accuracy, especially the effects of spatial resolution, has been investigated thoroughly for the steady-state procedure. For the cases reported thus far, grids of 180×60 unevenly spaced elements have been employed. This configuration has also been the standard mesh for the stationary calculations. For various Ra's we have checked the influences of different resolutions. This includes different numbers of elements and also different methods of grid refinement. In general, the size of the elements increases as a polynomial function in both the horizontal and vertical directions. They increase from the boundaries towards the center of the box and decrease symmetrically again toward the opposite edge. A short description of the refinement procedure is provided in Table I. For a more detailed description of the grid refinement algorithm, the reader is referred to Hansen and Ebel [22]. Here we give only a few examples of these tests. A summary of the mesh refinement can be found in Table I. For $Ra=10^8$ we obtained values of $Nu=72.011$ on 180×60 elements and 72.009 on a 350×90 element grid. For both grid configurations the size of the smallest element in the x and z directions has been 0.001. Another mesh with the same vertical structure as given above for the 60 vertical elements but with 450 evenly spaced elements in the horizontal direction (i.e., $x=0.004$) yields a value of $Nu=71.57$. An additional increase of the number of horizontal elements to 675 produced a Nusselt

TABLE I. Nusselt numbers for $\mathrm{Ra}=10^8$, as obtained for different finite-element grids. The symbols have the following meaning: N_x,N_z: number of elements in the x (z) direction; α_x,α_z: amplification factor in the x (z) direction; Δ_x,Δ_z: size of the smallest element in the x (z) direction; Δ_X,Δ_Z: size of the largest element in the x (z) direction. The size of the $(n+1)$th element is calculated from the nth element as $\Delta_{x,n+1}=\alpha_x^n\Delta_{x,n}$ in the x direction and as $\Delta_{z,n+1}=\alpha_z^n\Delta_{z,n}$ in the z direction. The amplification factors α_x and α_z are calculated from $\sum_{n=0}^{N_z/2}\alpha_z\Delta_z=0.5$ and $\sum_{n=0}^{N_x/2}\alpha_x^n\Delta_x=\lambda/2$. λ represents the aspect ratio of the box.

Mesh properties	Nusselt number
$N_x=180$, $N_z=60$ $\alpha_x=1.0413$, $\alpha_z=1.157$ $\Delta_x=0.0010$, $\Delta_X=0.0366$ $\Delta_z=0.0010$, $\Delta_Z=0.0687$	71.011
$N_x=350$, $N_z=90$ $\alpha_x=1.0156$, $\alpha_z=1.0884$ $\Delta_x-0.0010$, $\Delta_X=0.0148$ $\Delta_z=0.0010$, $\Delta_Z=0.0415$	72.009
$N_x=450$, $N_z=60$ $\alpha_x=1$, $\alpha_z=1.1570$ $\Delta_x=0.004$, $\Delta_X=0.004$ $\Delta_z=0.001$, $\Delta_Z=0.0687$	71.57
$N_x=675$, $N_z=60$ $\alpha_x=1$, $\alpha_z=1.1570$ $\Delta_x=0.002\,66$, $\Delta_X=0.002\,66$ $\Delta_z=0.001$, $\Delta_Z=0.006\,87$	71.83

number of Nu=71.83. Thus we can consider the agreement of these Nu values for different grids as excellent.

Time-dependent calculations in the high-Ra regime are much more difficult to test as far as convergence is concerned. The results reported here have been checked by two independent methods, the finite-element method and the spline method as described already in Ref. [15]. With the bicubic spline technique we have compared the solutions obtained on the different grids. The time-dependent solution for $\mathrm{Ra}=10^8$ in an aspect-ratio-1.8 box was calculated on 200×90 and 400×140 grid points. The kinetic-energy spectra for the both grids at the same time instant ($t=0.667\times10^{-4}$) are shown in Fig. 5. We first calculated the two-dimensional Cartesian, kinetic-energy spectra and then converted them into a one-dimensional spectrum in polar form:

$$E(k_r)=\frac{1}{2}\int_0^{\pi/2}[u^2(k_r,k_\vartheta)+w^2(k_r,k_\vartheta)]d\vartheta\,, \tag{13}$$

where u and w are the Fourier transforms of the horizontal and vertical velocities taken on the two-dimensional Cartesian wave-number space.

The kinetic-energy spectra $E(k_r)$ for $\mathrm{Ra}=3\times10^8$ and an aspect ratio of 1.8 were computed for the solution over 280×78 and 400×100 grid points. They are shown in Fig. 5 for $t=0.123\times10^{-3}$. The kinetic-energy spectra for the thermal convection in the hard turbulent regime exhibit a power-law decay [18] with a slope close to −2.

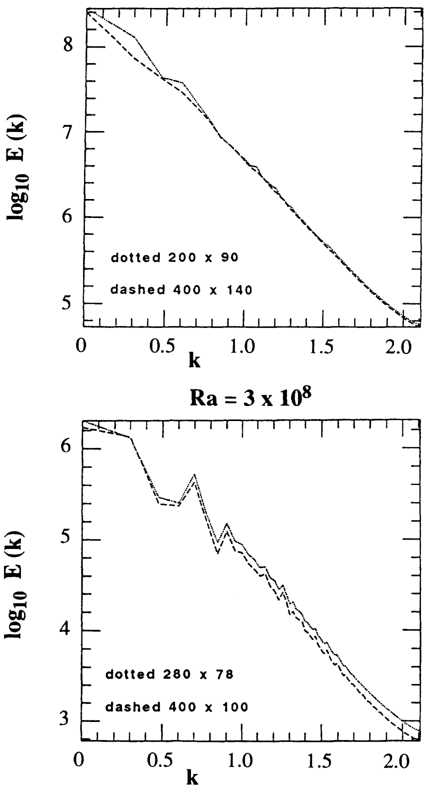

FIG. 5. Kinetic-energy spectra as a function of the wave number k_r for two different grids. The bicubic spline method was used. For $\mathrm{Ra}=10^8$ (top panel) meshes of 200×90 and 400×140 were compared, while for $\mathrm{Ra}=3\times10^8$ (bottom panel), 280×78 and 400×100 grid points were used.

With these high-resolution grids, spectra spanning more than two decades in wave number can be calculated. These spectra show that the kinetic energy decays by more than three orders of magnitude in these high-Ra simulations.

It is also important to compare the spatial resolution for the two configurations. The vorticity field is a good measure of the spatial accuracy, as it involves spatial derivatives. We compare the vorticity fields for $\mathrm{Ra}=10^8$ at $t=0.667\times10^{-4}$ (Fig. 6). Inspection shows that the details of the many vortices associated with plume instabilities are captured by both grids. Additionally, we took a stage from the evolution obtained by the finite-element model as an initial condition for a high-resolution run with the spline method. From monitoring the time history of Nu, the subsequent evolution of both runs shows excellent agreement. These comparison tests demonstrate that both methods work satisfactorily and that the numerical resolution is quite adequate.

A more detailed investigation of the statistical properties of the chaotic flow for $\mathrm{Ra}=3\times10^7$ is exhibited in Figs. 7(a) and 7(b). In Fig. 7(a) the time-history plot of Nu_t is displayed. The formation and eruption of plumes from the boundary layers produce a rather jagged time series. The same time series, plotted as a histogram, shows more clearly the statistical properties of the flow

[Fig. 7(b)]. The Nusselt numbers follow a Gaussian distribution around a mean value Nu_t. The solid line in Fig. 7(b) denotes the theoretical Gaussian distribution for the mean value Nu_t and the root-mean-squared (rms) deviations obtained from the run. Comparing the mean value of Nu_t and the value Nu_s from the corresponding steady state, we find the almost identical values of $\mathrm{Nu}_t=49.29$ and $\mathrm{Nu}_s=49.19$. Thus, the time-dependent evolution of the turbulent flow can be represented by a Gaussian distribution of the Nusselt numbers around a mean value Nu_s, as taken from the solution of the steady-state equations.

Another experiment, carried out at $\mathrm{Ra}=6\times10^7$, corroborates this finding. As shown in Figs. 8(a) and 8(b), we obtain a very similar picture for this Ra. The time history of the Nusselt number is represented by a Gaussian distribution with a mean value of $\mathrm{Nu}_t=59.84$ and a rms derivation of $\sigma=5.11$. Nu_s taken from the corresponding steady state is 61.22, thus again agreeing well with Nu_t.

A potential source of discrepancies between Nu_t and Nu_s is due to the inadequate length of the time series. The question of how long a model needs to be run in order to reach a statistically steady state remains open. While Balachandar, Maxey, and Sirovich used less than 5 overturns in their first work [38], more recent studies by Balachandar and Sirovich [10] are based on model runs with about 40 overturns. Vincent and Menneguzzi [19]

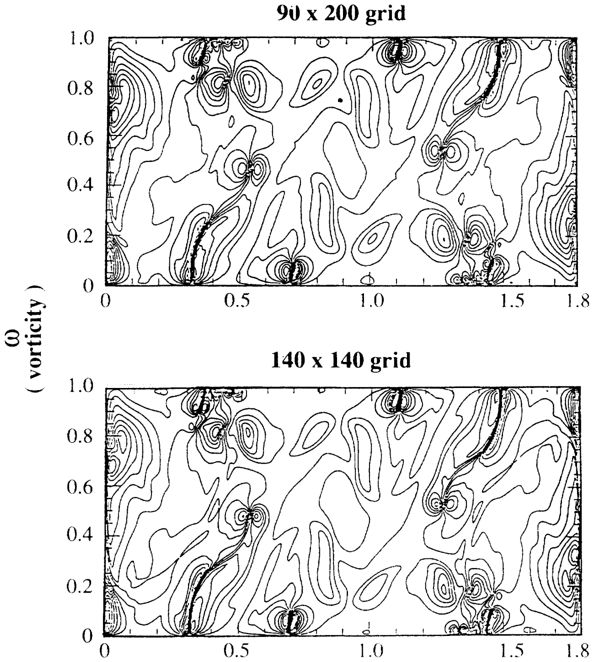

FIG. 6. Comparison of the vorticity fields at $\mathrm{Ra}=10^8$ for two different grids. The bicubic spline method was used with 90×200 and 140×400 meshes. The time instant is $t=6.67\times10^{-5}$.

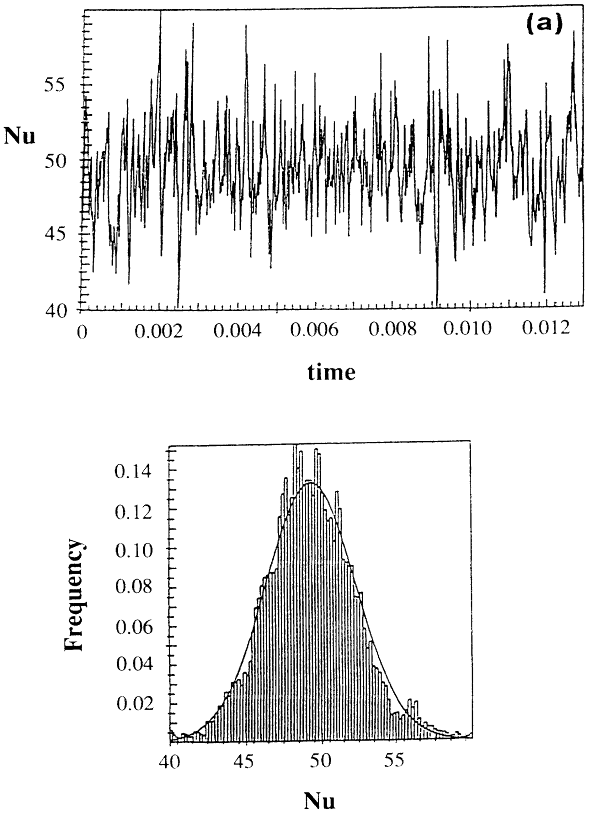

FIG. 7. Time history of $\mathrm{Nu}_{(t)}$ for $\mathrm{Ra}=3\times10^7$: (a) $\mathrm{Nu}_{(t)}$ for 80 overturns. The finite-element method was used with 90×30 grid points. (b) Histogram depicting the normalized frequency of occurrence for Nu in that time interval. One hundred bins were used in the sampling.

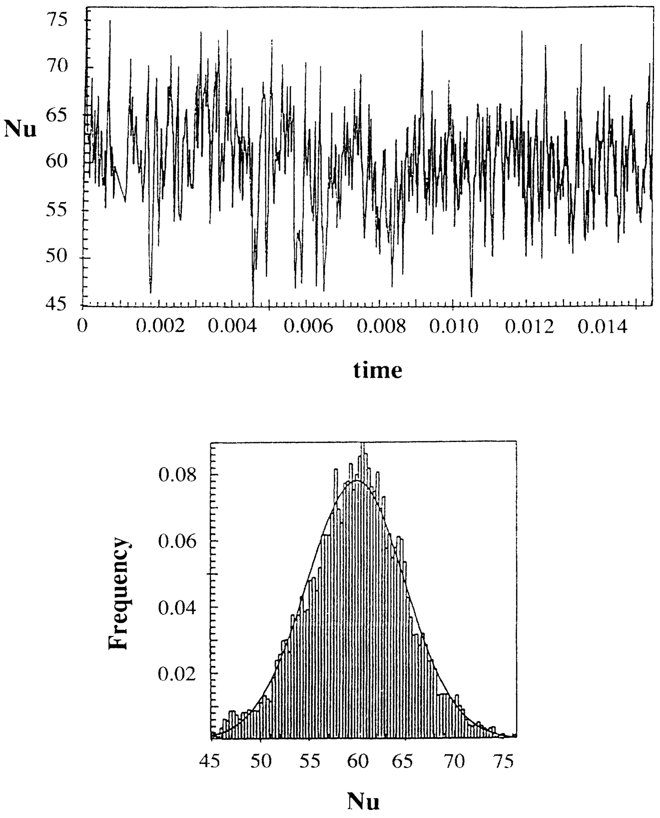

FIG. 8. Same as in Fig. 7 except $\mathrm{Ra}=6\times10^7$. One hundred forty overturns were included using a 90×30 grid.

argue that even a few tens of overturns might not be sufficient to determine statistical properties in the temporal domain. Adopting the definition of an overturn time [10] as

$$\tau = d / v_{\mathrm{rms}} \,, \tag{14}$$

where d and v_{rms} is the rms velocity, we have calculated about 100 overturns for $\mathrm{Ra}=3\times10^7$ and about 140 overturns for $\mathrm{Ra}=6\times10^7$. We note that Fig. 8 shows only the last portion of a much longer simulation.

It is illustrative to look at the shape of the histograms as a function of the length of the time series. Figure 9 shows the distribution of Nu for the case of $\mathrm{Ra}=6\times10^7$ when only a fraction of the time series is taken. Figure 9 displays the distribution of the Nu values for 4, 20, 40, and 80 overturns. Already after 4 overturns the mean value $\mathrm{Nu}_t=63.09$ is close to the final value, reflecting that many overturns have been calculated before in order to damp out transients. Clearly, the shape of the histograms changes with the length of the time series, as can be seen from Figs. 8(a) to 8(c). From 80 [Fig. 9(d)] to 140 [Fig. 8(b)] overturns, there is hardly any change in the shape of the distribution, indicating that a statistically stationary solution has been achieved.

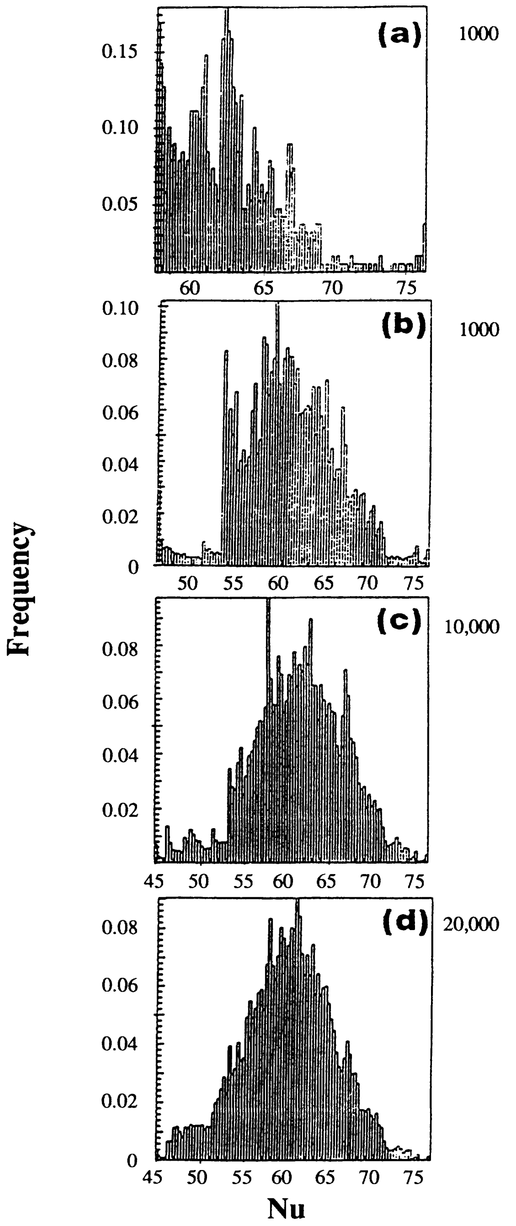

FIG. 9. Effects of length of time-interval on the normalized frequency of Nu occurrences. One-hundred bins were considered (a) after 4 overturns, (b) after 40 overturns, (c) after 40 overturns, and (d) after 80 overturns. Numbers adjacent to the panels denote the counting of time steps.

The close agreement of the Nu_t and Nu_s values has encouraged us to carry out a systematic investigation, which spans the Ra in the range of 10^6 and 10^9. The results obtained from the iteration procedure are summarized in Fig. 10(a). The Nu-Ra relation can be expressed in the form of the power law $\mathrm{Nu}_s=0.219\mathrm{Ra}^{0.315}$. Figure 9(b) shows the same relationship but also the values of Nu_t, as indicated by the symbols (squares for results from the finite-element models and solid circles for the spline method). The deviations of Nu_t values from the Nu_s

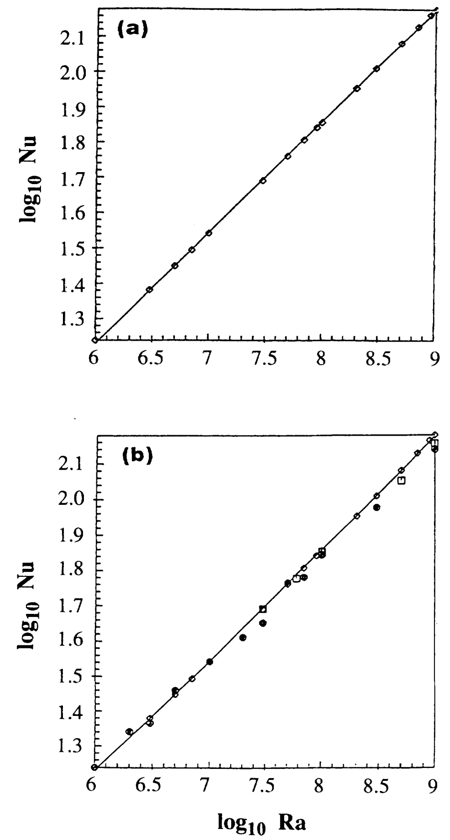

FIG. 10. Nu vs Ra: (a) steady-state and (b) steady-state and time-dependent results. Time-dependent finite-element results are in rectangles and time-dependent bicubic splines are in solid circles. All steady-state calculations were performed on a 180×60 finite-element grid. For time-dependent calculations and for Ra less than 6×10^7, a 90×30 grid was used, while for greater Ra, a 180×60 grid was employed. For the bicubic spline method we have used 70×37 for $\mathrm{Ra}=10^6$, 160×48 for $\mathrm{Ra}=10^7$, 200×90 for $\mathrm{Ra}=10^8$, and 400×140 for $\mathrm{Ra}=10^9$.

curve is solely due to the limited length of some of the time series. Some of the experiments, especially the circles for $\mathrm{Ra} > 10^7$, were run only for a few overturns, due to limited computer time. The kink in the Nu versus Ra curve found by Malevsky and Yuen [18] is probably caused by insufficient length of integration time. The longest run there [18] was for 12 to 15 overturns, whereas it is shown that at least 40 overturns are required to attain a statistical stationary state.

In Fig. 11 the distribution of the Nu values for the highest Ra of this study ($\mathrm{Ra} = 10^9$) is displayed. About 80 overturns were computed for this Ra. The histogram has not yet converged to a Gaussian distribution but the mean value $\mathrm{Nu}_t = 143.4$ already agrees very well with the Nu_s of 150 from the corresponding solution of the steady-state equations.

Within the range of Ra under investigation, a transition from soft to hard turbulence should occur [2,4]. Evidence for this transition is seen from the physical fields showing the transition from connected to disconnected plume structures [6,16]. However, our Nu-Ra relationship (Fig. 10) does not show any indication for such a transition. This result agrees with those of Solomon and Gollub [12], i.e., no kink in the Nu-Ra relationship. The exponent, as taken from our 2D numerical experiments, is significantly higher than those obtained in most laboratory experiments [2,12] but still below the theoretical value of $\frac{1}{3}$. In fact, many laboratory studies revealed exponents [38] of less than 0.3, while in numerical studies on convection, usually exponents higher than 0.31 for stress-free boundaries have been obtained. We believe that the reason for the difference in the scaling exponents is mainly due to the different boundary conditions, since in laboratory experiments rigid boundary conditions are commonly employed. Preliminary numerical experiments conducted for rigid boundary conditions support this view that different mechanical boundary conditions can influence the heat-transfer characteristics at high Ra.

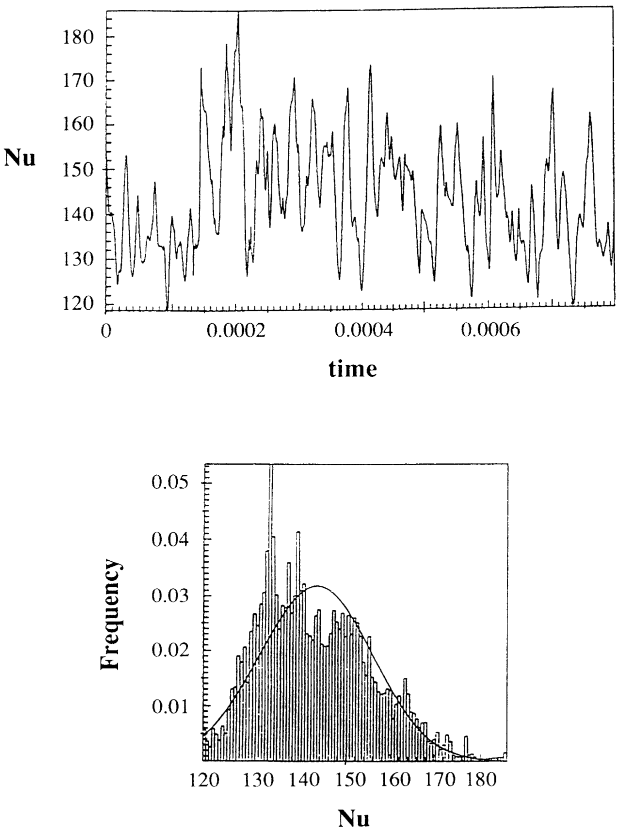

FIG. 11. Nu time history and histogram of Nu for $\mathrm{Ra} = 10^9$. Finite-element method was employed with a grid of 180×60 points.

Besides the Ra, Nu is also influenced by the aspect ratio of the flow [22,39,40]. In Fig. 12 we demonstrate the dependence of the Nusselt number Nu_s on the aspect ratio at $\mathrm{Ra} = 10^8$. The curve, agreeing almost perfectly with the asymptotic approach of Olson and Corcos [40] for Ra tending to infinity, exhibits a weak dependence of Nu_s on the aspect ratio λ at values of λ around unity but a strong dependence for larger aspect ratios. It is remarkable that the mean values Nu_t from the time-dependent calculation agree only with the stationary flow of the aspect ratio 1.8. For example, a steady state consisting of two rolls each with an aspect ratio of 0.9 in an aspect-ratio-1.8 box produces a Nusselt number of $\mathrm{Nu}_s = 97$ (Fig. 12) differing considerably from the value Nu_t of 71. We therefore conclude that the relevant scale governing the heat transport is the width of the box and that all the small-size instabilities do not contribute much at all to the global heat transport. In Fig. 13 we show the variation of the root-mean-squared velocity v_{rms} with Ra, as calculated from the stationary cases. As in the case for the Nu-Ra relation, we find here also a clear power-law dependence of the form $v_{\mathrm{rms}} = C\mathrm{Ra}^{\beta}$, with $C = 0.107$ and $\beta = 0.639$. This value of β is thus significantly lower than the theoretical prediction [8] of $\frac{2}{3}$ predicted for stress-free boundaries. However, the value of β_1 is consistent in the sense that the relationship $\beta_1 = 2\beta$, as predicted from boundary-layer theory, is nearly kept with $2\beta = 0.630$.

From the numerical experiments we can also measure the variation of the boundary-layer thickness δ as a func-

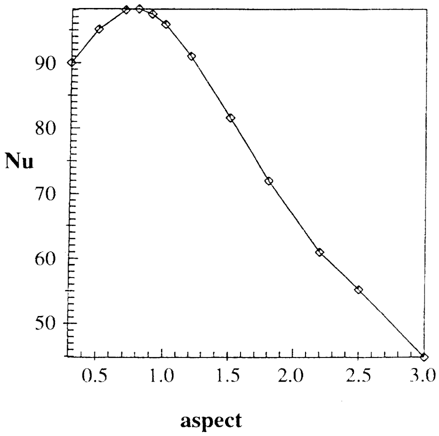

FIG. 12. Nu_s for steady-state solutions vs aspect ratio for $\mathrm{Ra} = 10^8$. Aspect ratio is defined to be width divided by depth. A grid of 60×180 points was used.

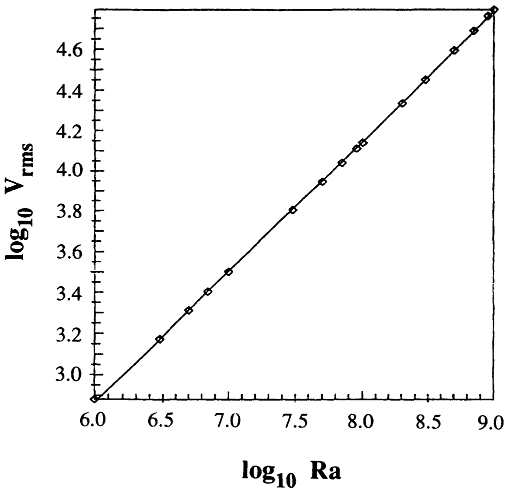

FIG. 13. Root-mean-squared velocity vs Ra for steady-state solutions. Otherwise, same as in Fig. 10.

tion of Ra in a direct manner. In order to be consistent with theory and previous numerical experiments [28], we define the boundary layer to be the depth over which the temperature drops by $\Delta T/2$. For determining this depth, we use the horizontally averaged temperature. The result for $10^6 < \mathrm{Ra} < 10^8$ is displayed in Fig. 14. The boundary-layer thickness δ is related to Ra by the power law $\delta = g\mathrm{Ra}^{\gamma}$, with $g = 3.90$ and $\gamma = -0.306$. This result is different from the boundary-layer with $-1/3$ for the exponent (see Eq. 10).

In the theoretical approach two assumptions are made about the structure of the thermal boundary layer. First, a temperature drop of $\Delta T/2$ is assumed to take place across the boundary layer and, second, the vertical heat transport is assumed to be purely diffusive within the boundary layer. The relation between Nu and δ [Eq. (11)] is based on these assumptions. Earlier numerical work [41] has demonstrated that a temperature drop of $\Delta T/2$ is not produced by pure diffusion. Figures 15(a) and 15(b) illustrate this point for a box of aspect ratio 1.8. Vertical profiles of the horizontally averaged temperatures are displayed for $\mathrm{Ra} = 10^6$ (Fig. 15(a)] and 10^8 [Fig. 15(b)]. The boundary layers, as defined by the $\Delta T/2$ criterion, are denoted by the hatched areas. Within the boundary layer the temperature profile deviates significantly from the conductive profile. Only a small part of the heat transfer is indeed governed by pure vertical diffusion; a much steeper temperature gradient is found in the other part of the boundary layer. The phenomenon of the overshoot in the temperature profile is well documented in the literature [35,40,41]. This is a consequence of cold material spreading out at the bottom, resulting in a mushroomlike shape, and is a dynamical feature produced by the large-scale circulation.

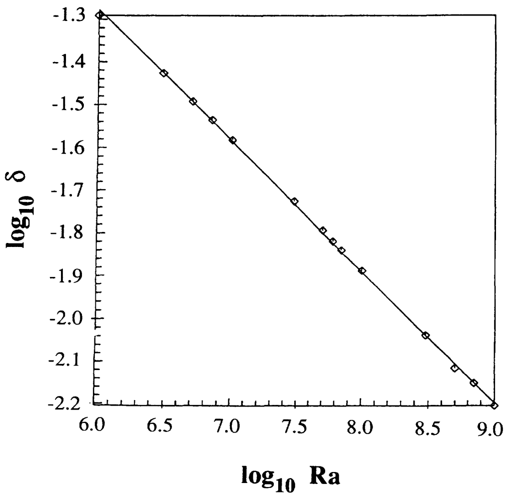

FIG. 14. Boundary-layer thickness δ vs Ra for steady-state solutions. Otherwise, same as in Fig. 10.

These numerical simulations demonstrate that the classical assumptions concerning thermal boundary layers do not hold for convection between stress-free boundaries. The thickness of the boundary layer may be defined differently as the layer over which vertical heat transport is purely conductive. However, this means that the temperature drop across the boundary layer would then be-

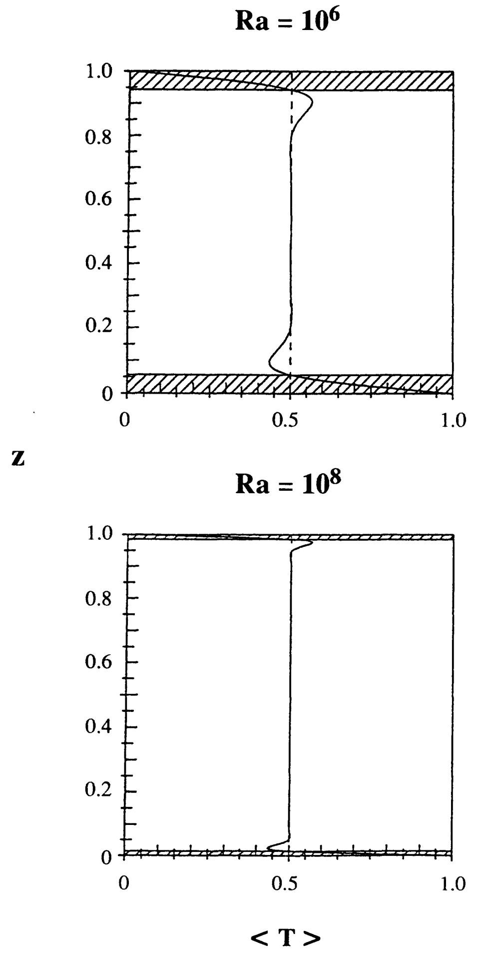

FIG. 15. Horizontally averaged temperature $\langle T \rangle$ vs depth for two steady-state solutions. Hatched area indicates boundary layer.

come a free parameter, being certainly less than $\Delta T/2$.

Comparing the properties of stationary convection and turbulent flows, we have so far only looked at global parameters, namely, the Nusselt number. In order to get a better understanding of the relation between global and local properties, we have analyzed the temperature fields and the vertical heat transport q as given by

$$q = wT - \frac{dT}{dz} \ . \tag{15}$$

We have compared in Figs. 16 and 17 the horizontal spectra of the temperature fluctuations T and the heat transport q for both steady-state and time-dependent solutions and $\mathrm{Ra}=10^6$ and 10^8. Two different depths ($z=0.0024$ and 0.3314) were considered. Time-dependent spectra (labeled t) were averaged in time in order to compare them with the steady-state (labeled s) spectra. Time averaging was performed for one overturn after the initial transients have been damped out. The spectra for heat transport (Fig. 16) show much closer agreement between the steady-state and time-dependent averaged cases than the thermal anomalies (Fig. 17). This is not surprising in view of our finding that the statistically stationary heat transport from time-dependent solutions approaches that of the steady state. We note that the agreement is closer for the low-wave-number portion of the q spectra. In the case of the T spectra, there are noticeable differences in the plume for $\mathrm{Ra}=10^8$ because of the presence of many small-scale structures in the interior of the hard turbulent flow (compare Figs. 3 and 4), while the agreement is better within the thermal boundary layer.

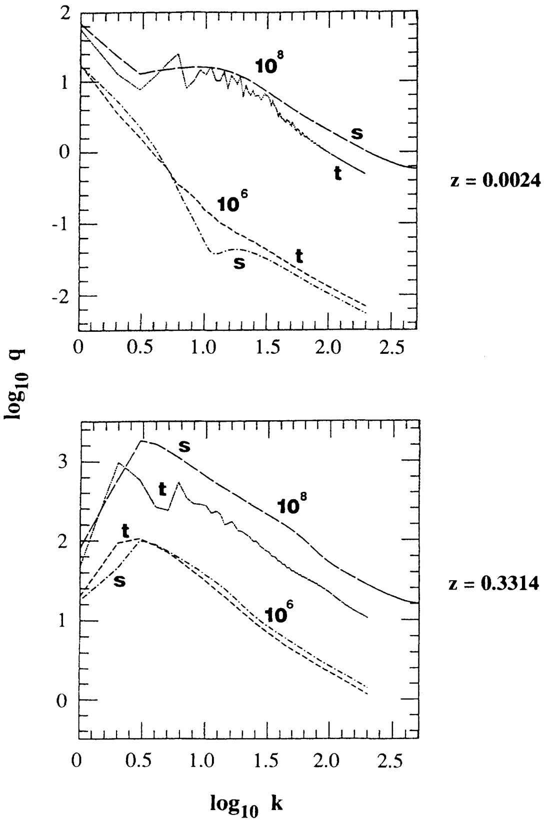

FIG. 16. Horizontal Fourier spectra of the heat transport q for steady-state and time-dependent solutions and $\mathrm{Ra}=10^6$ and 10^8. The letters "s" and "t" denote, respectively, steady-state and time-dependent solutions. Spectra for time-dependent solutions were taken after averaging over one overturn after several overturns have already been completed.

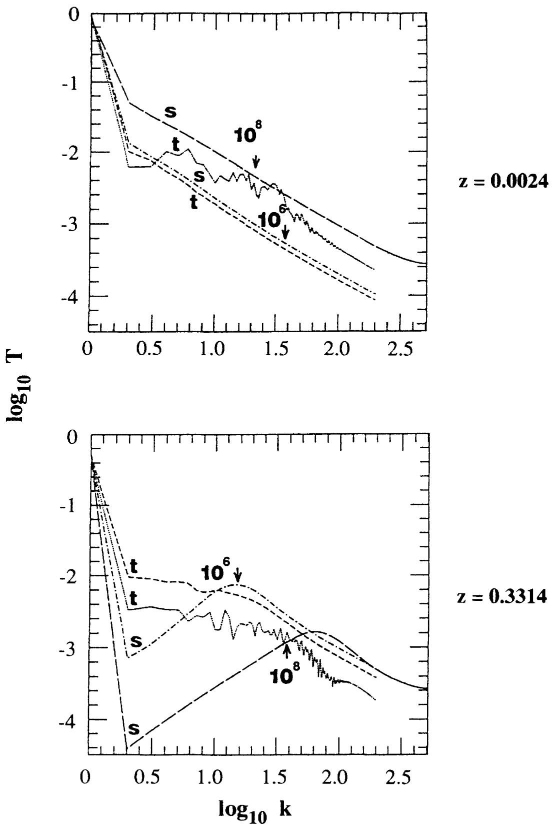

FIG. 17. Horizontal Fourier spectra of the temperature field at two different depths. Otherwise, same as in Fig. 16.

IV. CONCLUSIONS AND DISCUSSIONS

The main result of the paper is that stationary convection obtained from solving the steady-state equations for infinite-Prandtl-number fluids resembles the turbulent flow in a statistical sense. The values of the Nusselt numbers of the two-dimensional turbulent convection between stress-free boundaries follow a Gaussian distribution with a mean value Nu_t. A good coincidence is found between the Nu_t and the Nu_s values obtained from the corresponding stationary solution. The results have been confirmed by using different resolutions and particularly by using two independent numerical methods. A global analysis of the physical fields shows that plumes often break down into smaller pieces at Ra around a few times greater than 10^7, as described in previous three-dimensional and two-dimensional studies on the phenomenon of hard turbulence. It also reveals the existence of a persistent large-scale circulation with the relevant length scale being the width of the box. Since the heat transport is resembled in an averaged sense only by a stationary flow of the same aspect ratio, we conclude therefore that it is this large-scale circulation that governs the efficiency of heat transport in time-dependent convection.

The stationary solutions and thus the corresponding Nusselt numbers Nu_s can be calculated from the steady-state equations with an effort being about 10^4 times less than computing the mean value Nu_t for an actual time-dependent evolution. This equivalence of Nu_t and Nu_s allows for a detailed investigation of the scaling relations for turbulent convection for a wide range of Ra. In the range of Ra between 10^6 and 10^9, our study reveals the power-law indexes of Nu, v_{rms}, and δ are, respectively, $\beta=0.315$, $\beta_1=0.639$, and $\gamma=-0.306$. Compared to classical theory, the scaling exponent β is low but significantly higher than those values reported by DeLucca *et al.* [13], Castaing *et al.* [2], and Solomon and Gollub [14]. We did not find any evidence for a kink in the Nu-Ra relationship within this range of Ra [12], which would be a good indicator for the transition from soft to hard turbulence. We are led to conclude that the predominant occurrence of disconnected plumes, as observed in our numerical experiments and believed to be characteristic of the regime of hard turbulence [6,38], does not produce any changes in the Nu-Ra relationship.

The differences between our results for Nu and scaling exponents and those found in the aforementioned studies are due to the differences between stress-free and rigid boundary conditions. Busse [42] and references cited therein) has shown that for rigid boundaries, values of β lie between 0.28 and 0.29, while calculations for stress-free boundaries [24,28,43] generally have values greater than 0.31.

The scaling exponent for the rms velocity is likewise lower than the theoretical value but is consistent with boundary-layer theory, as it follows nearly the theoretically predicted relationship of $\beta_1=2\beta$.

The boundary-layer thickness can be defined rather arbitrarily. Commonly, it is defined as the layer in which the vertical heat transport is conductive and over which a temperature drop of $\Delta T/2$ occurs. Our study shows that these assumptions are not consistent. A boundary layer, as defined by the $\Delta T/2$ drop, depends inversely on Ra as predicted (exponent of -0.306 in instead of $-\frac{1}{3}$), but for this boundary layer the relation $\mathrm{Nu}=d/2\delta$ does not hold. A boundary layer, characterized by a temperature purely $\Delta T/2$, is not governed entirely by a conductive vertical heat transport. Conversely, the conductive layer would be thinner than δ and would show a temperature drop less than $\Delta T/2$. This finding may depend on the Prandtl number and on the aspect ratio. This certainly challenges the view of thermal boundary layers being at a marginally stable state. Instead, the thickness of the boundary layers may be determined by the balance of the conductive heat flux and the advective outward transport, as suggested by two recent theoretical works [44,45]. In this case the thermal boundary layer can be largely controlled by a sharing "wind," generated by the large-scale circulation.

The results reported here are all based on two-dimensional simulations and must therefore be verified for three-dimensional situations, in the near future, when much greater computing power becomes readily available with the arrival of second-generation massively parallel machines, such as the CM5.

ACKNOWLEDGMENTS

This research was supported by the German DFG and the Innovative Research Program of NASA. Supercomputing was done on both the NEC-SX3 at the Rechenzentrum of the University of Cologne and on the CRAY-2 at the Minnesota Supercomputer Center.

---

*Present address: Department of Theoretical Geophysics, University of Utrecht, TA-3508 Utrecht, The Netherlands.

[1] F. Heslot, B. Castaing, and A. Libchaber, Phys. Rev. A **36**, 5870 (1987).

[2] B. Castaing, G. Gunaraine, F. Heslot, L. Kadanoff, A. Libchaber, S. Thomae, X. Z. Wu, S. Zaleski, and G. Zanetti, J. Fluid Mech. **204**, 1 (1989).

[3] R. Krishnamurti and L. N. Howard, Proc. Natl. Acad. Sci. **78**, 1981 (1981).

[4] M. Sano, X. Z. Wu, and A. Libchaber, Phys. Rev. A **40**, 6421 (1989).

[5] L. Sirovich, S. Balachandar, and M. R. Maxey, Phys. Fluids A **1**, 1911 (1989).

[6] U. Hansen, D. A. Yuen, and S. E. Kroening, Phys. Fluids A **2**, 2157 (1990).

[7] L. N. Howard, in *Proceedings of the Eleventh International Congress of Applied Mechanics, Munich, 1966*, edited by H. Goertler (Springer-Verlag, Berlin, 1966), p. 1109.

[8] D. L. Turcotte and E. R. Oxburgh, J. Fluid Mech. **28**, 29 (1967).

[9] R. J. Goldstein, H. D. Chiang, and D. L. See, J. Fluid Mech. **213**, 111 (1990).

[10] S. Balachandar and L. Sirovich, Phys. Fluids A **3**, 919 (1991).

[11] X. Z. Wu, Ph.D. thesis, University of Chicago, 1991.

[12] T. H. Solomon and J. P. Gollub, Phys. Rev. A **43**, 6683 (1991).

[13] E. E. DeLucca, J. Werne, R. Rosner, and F. Cattaneo, Phys. Rev. Lett. **64**, 2370 (1990).

[14] T. H. Solomon and J. P. Gollub, Phys. Rev. Lett. **64**, 2382 (1990).

[15] A. P. Vincent, U. Hansen, D. A. Yuen, A. V. Malevsky, and S. E. Kroening, Phys. Fluids A **3**, 2222 (1991).

[16] U. Hansen, D. A. Yuen, and S. E. Kroening, Geophys. Astrophys. Fluid Dyn. **63**, 67 (1992).

[17] K.-H. Winkler, J. W. Chalmers, S. W. Hodson, P. R. Woodward, and N. J. Zabusky, Phys. Today **40**, 28 (1987).

[18] A. V. Malevsky and D. A. Yuen, Phys. Fluids A **3**, 2105 (1991).

[19] A. P. Vincent and M. Meneguzzi, J. Fluid Mech. **225**, 1 (1991).

[20] R. Robert and J. Sommeria, J. Fluid Mech. **229**, 291 (1991).

[21] U. Hansen and A. Ebel, Geophys. J. **94**, 181 (1988).

[22] U. Hansen and A. Ebel, Phys. Earth Planet. Int. **36**, 374

(1984).

[23] B. Blankenbach, F. H. Busse, U. R. Christensen, L. Cserepes, D. Gunkel, U. Hansen, H. Harder, G. Jarvis, M. Koch, G. Marquart, D. Moore, P. L. Olsen, H. Schmeling, and T. Schnaubelt, Geophys. J. Int. **98**, 23 (1989).

[24] G. Schubert and C. A. Anderson, Geophys. J. R. Astron. Soc. **80**, 575 (1985).

[25] E. M. Parmentier, D. l. Turcotte, and K. E. Torrance, J. Geophys. Res. **80**, 4417 (1975).

[26] F. H. Busse, J. Math. Phys. **46**, 140 (1967).

[27] L. Onsager, Nuovo Cimento Suppl. **6**, 279 (1949).

[28] G. T. Jarvis and W. R. Peltier, Geophys. J. R. Astron. Soc. **68**, 385 (1982).

[29] L. P. Solheim and W. R. Peltier, Geophys. Astrophys. Fluid Dyn. **53**, 205 (1990).

[30] U. R. Christensen, Geophys. Astrophys. Fluid Dyn. **46**, 93 (1989).

[31] W. V. R. Malkus, Proc. R. Soc. London, Ser. A **225**, 196 (1954).

[32] G. T. Jarvis, Phys. Earth Planet. Int. **36**, 305 (1984).

[33] A. P. Vincent and D. A. Yuen, Phys. Rev. A **38**, 328 (1988).

[34] E. W. Bolton, F. H. Busse, and R. M. Clever, J. Fluid Mech. **164**, 469 (1986).

[35] J. Jimenez and J. A. Zufiria, J. Fluid Mech. **178**, 53 (1987).

[36] G. A. Houseman, Nature **332**, 346 (1988).

[37] G. J. F. van Heijst and J. B. Flor, Nature **340**, 212 (1989).

[38] S. Balachandar, M. R. Maxey, and L. Sirovich, J. Sci. Comput. **4**, 219 (1989).

[39] D. C. Threlfall, J. Fluid Mech. **67**, 17 (1975).

[40] P. L. Olson and G. M. Corcos, Geophys. J. R. Astron. Soc. **62**, 195 (1980).

[41] F. M. Richter and D. P. McKenzie, J. Geophys. Res. **86**, 1738 (1981).

[42] F. H. Busse, in *Hydrodynamic Instabilities and the Transition to Turbulence,* 2nd ed., edited by H. L. Swinney and J. P. Gollub (Springer-Verlag, Berlin, 1985), p. 97.

[43] T. Y. Chu and R. J. Goldstein, J. Fluid Mech. **60**, 141 (1973).

[44] B. I. Shraiman and E. D. Siggia, Phys. Rev. A **42**, 3650 (1990).

[45] S. Zaleski, C. R. Acad. Sci. Paris **313**, Ser. 2, 1099 (1991).

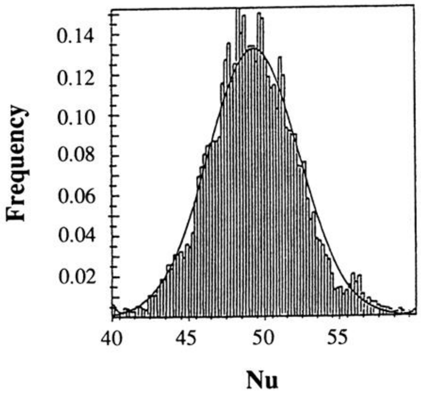

FIG. 7. Time history of $\mathrm{Nu}_{(t)}$ for $\mathrm{Ra}=3\times 10^7$: (a) $\mathrm{Nu}_{(t)}$ for 80 overturns. The finite-element method was used with 90×30 grid points. (b) Histogram depicting the normalized frequency of occurrence for Nu in that time interval. One hundred bins were used in the sampling.

time

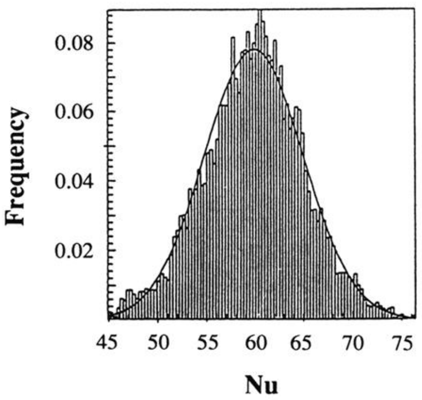

FIG. 8. Same as in Fig. 7 except $Ra = 6 \times 10^7$. One hundred forty overturns were included using a 90×30 grid.

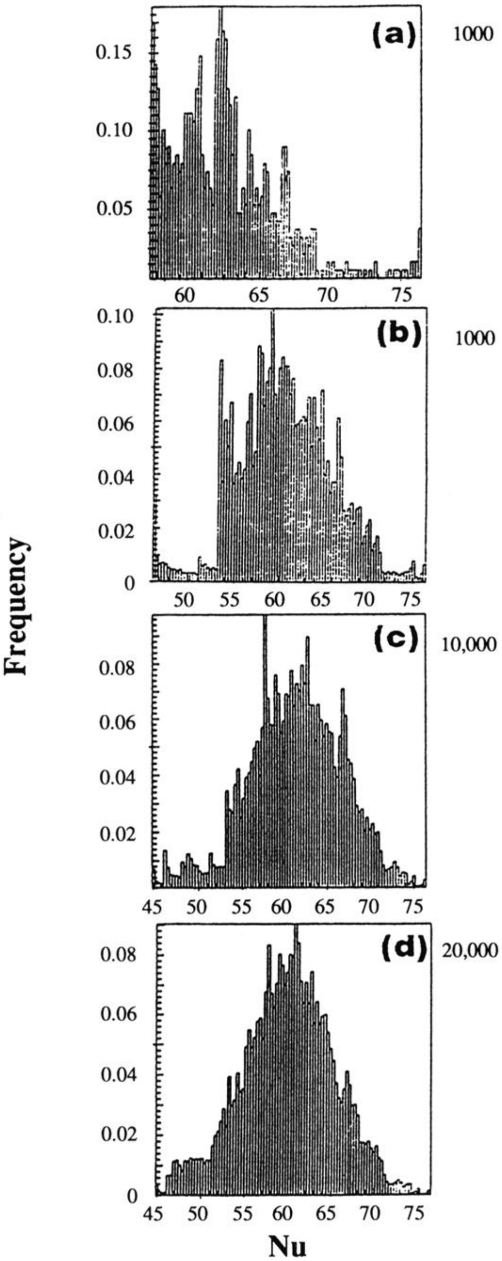

FIG. 9. Effects of length of time-interval on the normalized frequency of Nu occurrences. One-hundred bins were considered (a) after 4 overturns, (b) after 40 overturns, (c) after 40 overturns, and (d) after 80 overturns. Numbers adjacent to the panels denote the counting of time steps.